Thèse de doctorat

Characterization of SuperNEMO demonstrator calorimeter timing performance
Study of 208Tl background rejection influence on the 0nubb decay sensitivity

CLOÉ GIRARD-CARILLO

Composition du Jury :

***
***   Président

Alessandra Tonazzo
APC - Paris   Rapporteur

Mark C. Chen
Queen's University   Rapporteur

Christine Marquet
CENBG - Bordeaux-Gradignan   Examinateur

Laurent Simard
LAL - Orsay   Directeur de thèse

Mathieu Bongrand
LAL - Orsay   Co-directeur de thèse

Contents

The SuperNEMO demonstrator

2.1 The SuperNEMO technology

The Neutrino Ettore Majorana Observatory (NEMO) is an international collaboration of scientists searching for the yet never-observed $0\nu\beta\beta$ decay. This collaboration began in 1989 with a first device based on an innovative technology coupling a charged particles tracking chamber and a calorimeter measuring the particle energies. Since then, 3 detectors based on the same technology were installed and collected data in the Modane Underground Laboratory (Laboratoire Souterrain de Modane in French), a subterranean laboratory located in the Fréjus road tunnel, below the Fréjus peak. In particular, the third generation of detector, the so-called NEMO-3 experiment, which had been operating from 2003 to January 2011, derived a lower limit on the half-life of $0\nu\beta\beta$ decays of enriched Molybdenum (^{100}Mo) of $T_{1/2}^{0\nu} > 1.1 \times 10^{24}$ years at the 90% Confidence Level, under the hypothesis of light Majorana neutrino exchange. Depending on the model adopted for calculating nuclear matrix elements, the limit for the effective Majorana neutrino mass lies in the range $\langle m_{\beta\beta}\rangle < [0.33 - 0.62]$ eV. Therefore, if existing, the $0\nu\beta\beta$ decay would remain an extremely rare event. The NEMO experiments have then been designed to be ultra-low background detectors, reaching high radiopurity levels, and efficiently removing background events thanks to the tracko-calo technology.

Based on a similar principle, the SuperNEMO detector stands as the successor of NEMO-3, and is expected to set a lower limit of $T_{1/2}^{0\nu} > 1 \times 10^{26}$ years with 100 kg of ^{82}Se in 5 years of data acquisition. In order to prove the NEMO technology is scalable to such considerable masses of isotope, while remaining an ultra-low background detector, the SuperNEMO demonstrator had been designed with a reduced mass of $\beta\beta$ isotope, being 6.23 kg of ^{82}Se. Installation has begun at LSM in 2015. Since then, the sources have been installed, the tracker and calorimeter were assembled. It was an honour to personally participate in the detector closure, the 22 November 2018 (Fig. 2.1). The demonstrator is currently in the commissioning phase: the calorimeter is fully calibrated while the tracker enters in this important phase.

Figure 2.1: Last picture of the SuperNEMO demonstrator before closing it, the 22nd of November 2018. The picture is taken from one side of the detector, facing the other side. We can distinguish on the right the front of one of the two calorimeter main walls, and on the left one of the two tracker chambers.

2.1.1 Detection principle

The SuperNEMO demonstrator, in the manner of NEMO-3, combines tracking and calorimetry technologies to record the full event kinematics and measure the particle energies. It is designed to search for the $0\nu\beta\beta$ decay which, if observed, would reveal the Majorana nature of the neutrino particle, opening the door of physics beyond the Standard Model, with huge implications in numerous physics research fields (in cosmology, for instance). The SuperNEMO demonstrator is 6 meters long, 3 meters tall and 2 meters deep. It is the first of the 20 modules that will make up the final detector. This unique technology allows the experiment to characterise with a significant performance its own background, placing the detector in the ultra-low background category of experiments.

In Fig. 2.2 is drawn a simplified scheme of the SuperNEMO demonstrator. In order to ease the naming of the different areas of the detector, the collaboration has decided to label each part as *French*, *Italian*, *tunnel* or *mountain* sides, given with respect to the orientation of the detector in the underground laboratory. The isotope $\beta\beta$ emitter is distributed within ultra thin foils, at the centre of the detector. Therefore, for the same detector size, the mass of isotopes studied with this technology is lower than for experiments using liquid scintillators or TPCs. However, for the SuperNEMO design, the source is separated from the detector which allows to study any $\beta\beta$ isotope as long as it can be set up in solid thin foils, making this technology very interesting for the search of the $0\nu\beta\beta$ decay. We also schematise an emission of two negatively charged particles from the source, exiting in opposite directions for this particular case. The design of SuperNEMO as a layer of successive sub-detectors makes it possible to collect numerous information on
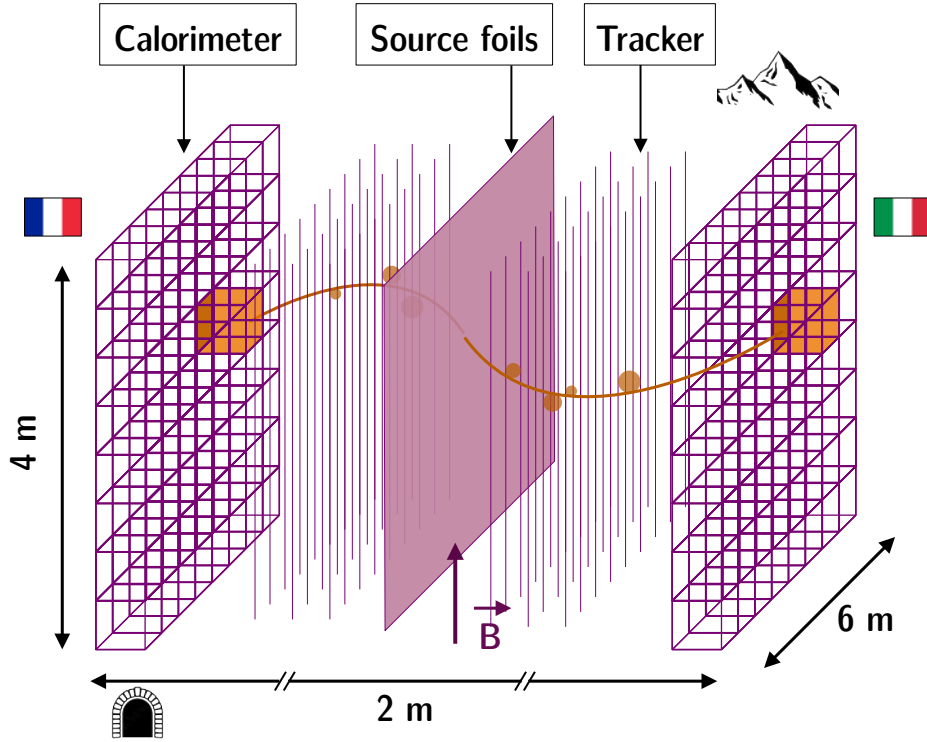
Figure 2.2: Scheme of an open view of the SuperNEMO demonstrator (not to scale). An example of emission from the source foils of two negatively charged particles is drawn. Each side of the tracker is labelled as French, Italian, tunnel or mountain side.

the emitted particle. When crossing the wire chamber, the charged particle ionises the gas, and the arrival time of the signals on the anode and copper rings allows the track reconstruction. The detector is surrounded by a copper coil, delivering a magnetic field inside the wire chamber. The few MeV particle trajectories are bent, allowing to discriminate electrons from positrons. Muons have too much energy for their trajectory to be bent by a magnetic field of this intensity. The α particles interact too quickly so their track in the tracker are too short to be curved, but can still be recognised precisely because of the length of their track (a few cells long). Although the energy resolution and detection efficiency are modest compared to germanium or bolometer experiments, it is compensated by the powerful particle identification allowing to identify events coming from natural radioactive decays. Therefore, the tracking technology makes it possible to discriminate electrons from positrons (with the trajectory curvature), to identify γ particles (corresponding to an energy deposit inside the calorimeter without any associated track), and to tag delayed α particles (characterised by a short delayed track inside the wire chamber). The particle ends up in one of the scintillator blocks, where the collection of deposited charge by a photomultiplier tube (PMT) allows the incident particle energy measurement. All electric signals are sent to the electronic boards where they are sampled and recorded for a later off-line analysis.

In addition to the search for the $0\nu\beta\beta$ decay, the SuperNEMO technology is

suitable for the search for other processes like double beta decays to excited states of the daughter nucleus that can be studied in dedicated channels (two-electrons and one/two gamma particles). Thanks to the topological informations brought by the successive sub-detectors (single electron energy and emission angle between them), if the $0\nu\beta\beta$ signal is observed, the SuperNEMO technology would also have the ability to discriminate between different hypothesised underlying mechanisms, allowing to investigate physics beyond the Standard Model.

In the following we describe in detail the successive layers of the SuperNEMO demonstrator, from the $\beta\beta$ emitter source foils to the electronic boards where the signal is sampled.

2.1.2 The source foils

Choice of isotope

There are about 30 double beta emitters, some of which can be created in laboratory if an enrichment technique exists, for physics research purposes. The choice of the isotope is directed by several factors and experimental constraints. Although this choice is specific to each detector, some constraints are common to all $0\nu\beta\beta$ experiments.

- The energy transition $Q_{\beta\beta}$: a significant background coming from natural radioactivity is the γ of 2.615 MeV emitted after the β disintegration of ^{208}Tl. Also, ^{214}Bi isotope disintegrations have a high available energy with $Q_\beta = 3.27$ MeV. Therefore, a high $Q_{\beta\beta}$ would help to guaranty the experiment to be free from radioactive background.

- The phase space factor and the nuclear matrix elements: as described in Chapter 1, the $0\nu\beta\beta$ half-life depends on these two parameters. The higher they are, the more signal events are expected for a given data acquisition time. Unfortunately, the uncertainties that exist on the calculation on the nuclear matrix elements prevent us from reaching a clear conclusion on the isotope choice.

- The $2\nu\beta\beta$ half-life: this process represents an unavoidable background for the search for $0\nu\beta\beta$. Then, the higher the half-life of this process, the less $2\nu\beta\beta$ events are expected.

- The natural abundance: The higher it is, the more we can produce substantial quantities of the enriched isotope.

- Ease of enrichment: although it is not a measurable quantity as previous requirements, known purification techniques must be applicable to the isotope considered to reach high quantities of $\beta\beta$ emitter.

In Tab. 2.1 are given some of the $\beta\beta$ emitter characteristics presented above. ^{82}Se was chosen for SuperNEMO because of its high transition energy, and preferred to ^{100}Mo because of its higher $2\nu\beta\beta$ half-life (by a factor ~ 13). Its nuclear phase space factor and natural abundance are satisfying and its enrichment is feasible using classical technique (centrifugation).

Isotope	$Q_{\beta\beta}$ (MeV)	$G_{0\nu}$ (10^{-15} y^{-1})	$T_{1/2}^{2\nu}$ (y)	η (%)
^{48}Ca	4.273	24.81	6.37×10^{19}	0.187
^{76}Ge	2.039	2.363	1.926×10^{21}	7.8
^{82}Se	2.995	10.16	9.6×10^{19}	9.2
^{96}Zr	3.350	20.58	2.35×10^{19}	2.8
^{100}Mo	3.035	15.92	6.93×10^{18}	9.6
^{116}Cd	2.809	16.70	2.8×10^{19}	7.6
^{130}Te	2.530	14.22	6.9×10^{20}	34.5
^{136}Xe	2.458	14.58	2.165×10^{21}	8.9
^{150}Nd	3.367	63.03	9.11×10^{18}	5.6

Table 2.1: $\beta\beta$ emitter used in current $0\nu\beta\beta$ search. $Q_{\beta\beta}$, phase space factor, $2\nu\beta\beta$ half-life and natural abundance are given.

Source foils production

The ^{82}Se isotope is enriched and purified by the ITEP laboratory in Russia. Two purification techniques have been employed, given in Tab. 2.2. Approximate

Enrichment technique	^{82}Se quantity (kg)	Number of foils
Double distillation	$\sim 2+1.5$	$\sim 11+8$
Reverse chromatography	~ 3	~ 15

Table 2.2: Different purification techniques and corresponding approximate quantity of ^{82}Se isotope. Two batches of ^{82}Se have been produced through double distillation.

isotope quantities are given for each technique. A total of 6.23 kg of ^{82}Se powder have been produced and purified. After this purification step, the ^{82}Se is ground down to a fine powder (50 μm grains) and mixed with a radio-pure glue.

To shape the ^{82}Se powder into the final SuperNEMO source foils, two distinct designs have been tested, one by ITEP and the other by the LAPP laboratory in Annecy (Fig. 2.3).

- ITEP implemented the same technique as for NEMO-3 source foils, by smearing the ^{82}Se+glue mixture between two 12 μm thick Mylar backing films, creating 3 meters long foils. The Mylar is perforated by irradiation, allowing the mixture to dry and better adhere to the film.

- The LAPP team split up the foils in several pads: two Mylar sheets are heat welded together to host the several pads.

The principal interest in designing the sources that thin is to maximise the chances of the electrons produced inside the source to escape it, to be detected by the successive sub-layers. Moreover, thinner sources reduce electron energy losses inside the source, and thus their fluctuations, which also contributes to the global energy resolution of the detector. In addition, the collaboration made this design choice in order to leave the possibility of easy isotope change in the future. Finally, the 6.23 kg of ^{82}Se have been distributed into 34 source foils each of them measuring
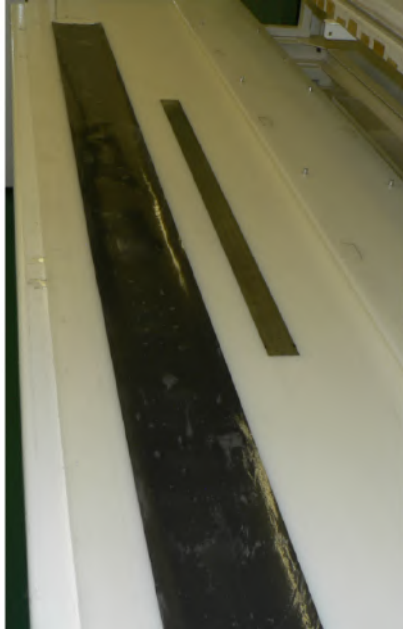
(a) ITEP style foils.
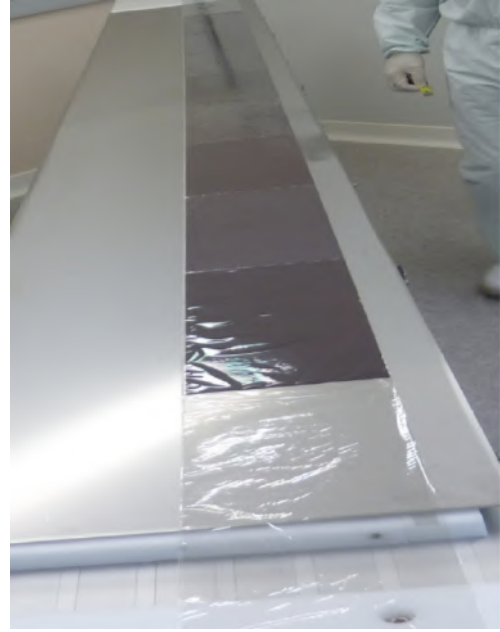
(b) LAPP style foils.

Figure 2.3: Two designs of source foils, ITEP (left) and LAPP (right).

135.5×2700 mm. The thickness of the produced sources will be precisely measured by the collaboration and are expected to be [Combien ?].

Source foils installation

Each strip was fasten to the source frame which measures 4.857 meters large and 2.7 meters high. The source foils have been installed the 24 September 2018. The original plan was to place the ITEP sources next to each other and to do the same for the LAPP sources. Unfortunately, some of the sources had to be relocated because of source shape issues (in particular, some sources were in contact with the Bismuth calibration sources, discussed in Sec. 2.1.6). The final position decided for the source foils are pictured in Fig. 2.4, where we can see the alternation of ITEP and LAPP sources. The final shape of the sources differs between the two types of sources: ITEP sources appear slightly curved on the image. This probably happened when the sources were drying, because of the glue mixed with the ^{82}Se powder. We can also distinguish the presence of the vertical wires of the tracker before the sources, discussed in next sub-section. Each source curvature have been precisely measured using a laser tracking system, for a future precise description of the sources geometry and its integration in the reconstruction software. I was part of the team that carried out the first curvature measurements after sources integration in Modane.

- Annexe position des sources

- dire pq deux techniques : cf thèse Delphine (radiopurity)

- mesure de radiopureté, BiPo ici ?

Figure 2.4: Final source foils position. The ITEP foils (one-piece long foils) and LAPP foils (divided in pads) are easily distinguishable.

2.1.3 The tracker

The tracker is a detector aiming at measuring the charged particle three-dimensional trajectories, through their electromagnetic interaction with the gas filling the tracking chamber. This sub-detector allows for efficient background rejection through the identification of particles, by making sure the event is composed of exactly two electrons. The reconstruction of the vertices on the source makes it possible to identify highly contaminated areas, the so-called *hot spots* of the experiment, and to reject them with appropriate cut-offs. The SuperNEMO tracker is divided into two halves, one on each side of the source frame, to measure particles coming out from the source in all possible directions. It consists of a wire chamber filled with a gas mixture, operating in Geiger regime.

Geiger counters

In Fig. 2.5 is schematised the basic operation principle of a Geiger cell. When a particle goes through the gas in which the cell is immersed, it ionises it all along its path, creating positive charges on one hand (heavy ions) and negative on the other hand (electrons). As a high electric potential is applied between the anodic wire and field wire, the freed electrons drift towards the anodic wire, and the ions towards the other one. When the ionisation electrons come close to the central wire, the electric field becomes so high that the accelerated electrons can themselves ionise the gas, creating electronic avalanches until the wire is reached. Other avalanches are created all along the anode wire by de-excitation and recombination
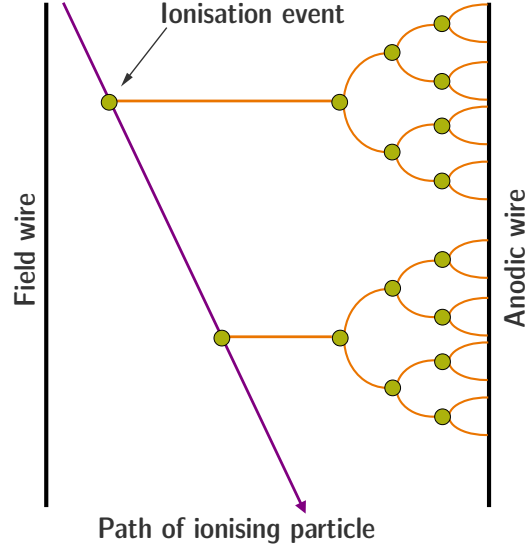
Figure 2.5: The principle of a Geiger cell illustrated with one central anodic wire and one field wire.

of UV photons. The longitudinal position is obtained with the time needed for these avalanches to reach both ends of the wire. The Geiger mode is reached when the avalanches created by the electrons are saturated: increasing the voltage does not increase the collected charge. This is the so-called *Geiger plateau*, which provides a very high detection efficiency ($> 99\%$).

SuperNEMO cells

A minimal amount of material is required inside the tracker chambers, for the particles to cross freely the detector with limited energy losses and reduced multiple scatterings. However, a minimal distance between the tracker wires is required in order to efficiently collect the charges coming from gas ionisation. Taking into account the tracker spatial resolution needs and the constraints on gas mixture composition, the decision was made to design Geiger cells as in Fig; 2.6, with one central anodic wire (stainless steel, 40μm in diameter) and 12 surrounding field wires (stainless steel, 50μm in diameter). Each cell has a diameter of 4.4 cm. Two copper rings, of 4 cm diameter and 4 cm long, are placed on both ends of each cell, allowing the cessation of the avalanches. In total, the tracker chamber is composed of 2034 Geiger cells of 3 m long, divided in 9×113 layers, parallel to the source strips. The detection of the anodic signal allows to measure the radial distance (the minimal distance of the particle from the anode) whereas the detection of the cathodic signals by both cathodic rings permits a longitudinal reconstruction (the position along the cell axis). The latter is obtained with the time needed for these avalanches to reach both ends of the cell. In the SuperNEMO operating conditions, a few micro seconds elapse between the creation of the first ionisation electron and the creation of the first avalanche, after which the avalanche is expected to spread through a cell in about 40 μs [7]. The times at which an electron passes nearby tracker cells are reconstructed using the calorimeter arrival time as a reference.

Figure 2.6: Sketch of a SuperNEMO Geiger cell, in transverse view (left) and side view (right, the sketch is rotated of 90° as the Geiger cells are vertical in the SuperNEMO demonstrator). The anodic central wire is represented at the centre in red. Field wires, in black, surround it to form 4.4 cm large and 3 m long Geiger cells. On the right the copped rings are also represented by orange stripes on each side of the wires.

As we said, the behaviour of a Geiger cell depends on the voltage applied. For the SuperNEMO cells, the Geiger plateau is located around 1800 V and is ~ 300 V-wide [8]. However, the exact voltage to be applied to each cell depends on their individual properties, and will have to be determined and set up after the tracker commissioning phase.

Gas mixture

The gas mixture is decisive for the wire chamber operation. For the SuperNEMO chambers, it is composed as follows:

- Helium is the main component of the gas mixture, which is ionised by incident radiations. As an inert gas, it does not react with the detector sensitive parts.

- Argon (1%) enhances the propagation of avalanches along the anode wires thanks to its lower ionisation energy.

- Ethanol (4%) is used as a quenching agent, stopping the successive discharges.

This gas composition guarantees a medium with a low Z number in order to minimise the energy losses and particle multiple scatterings for the electrons crossing the chamber.

Tracker installation

Each tracker side is divided in two C-sections (named in this way according to the C-shape of each section) assembled at UCL's Mullard Space Science Laboratory. They were delivered individually and integrated in Modane to form the two tracker chambers. In Fig. 2.7 is given a picture of the tracker after its integration to the detector. The bottom copper rings are noticeable and indicate the presence of the Geiger cells whose wires are too thin to be visible on the picture. After installation, some meticulous work were achieved to remove few wires damaged during transport.

Figure 2.7: Inside view of the tracker (with me standing in the foreground), before detector closing, on the day of the wire check, looking for possible broken wires at the base of the copper rings.

The tracking part of the demonstrator enters the commissioning phase in November 2020. Among other, each cell will have to be characterised, and is expected to have a 0.7 mm radial and 1 cm vertical spatial resolutions.

Gas sealing

A constant over-pressure is kept inside the tracker, which is imperative to maintain the right gas mixture, without infiltration of outside air. Indeed, if atmospheric air enters the gas detector, its properties can be disturbed. For example, the quenching may become too strong and the signal can not be properly transmitted through the gas. Therefore, once the tracker was integrated into the detector, a huge effort was achieved by the entire collaboration to seal it. In the case of SuperNEMO, it is also necessary that the detector is sealed to prevent helium from escaping and penetrating into the vacuum tubes of the PMTs. As a PhD student in the collaboration, I had the opportunity to participate in much of this work. The different techniques used to seal the detector are discussed in detail in Sec. 2.1.9.

2.1.4   The calorimeter

The $2\nu\beta\beta$ is an irreducible background for the $0\nu\beta\beta$ decay. Both these $\beta\beta$ decays have the same signature in the tracker, with two electrons emitted. The only way for the SuperNEMO technology to distinguish them is to measure the two electrons

individual energies. In order to achieve the target sensitivity, the calorimeter R&D program for SuperNEMO has covered three main areas of study: geometry, energy resolution and radiopurity. The two firsts are discussed in this sub-section, while the last one is detailed in Sec. 2.1.6.

- As shown in Fig. 2.2, the SuperNEMO calorimeter is segmented to measure the individual energies. A compromise has been reached between a high granularity and the minimisation of dead zones. Also, mainly for financial considerations, the number of electronic channels has to be reasonable.

- The lower the energy resolution, the more $2\nu\beta\beta$ and $0\nu\beta\beta$ energy spectra can be discriminated. In order to achieve the target sensitivity, the energy resolution of the SuperNEMO calorimeter is required to be around 8% FWHM at 1 MeV for electrons. The requirement for the time resolution is set to be σ_t = 400 ps at 1 MeV for external background rejection purposes (to discriminate between two-electron internal events from those that originate outside of the detector and then cross its active volume to imitate $0\nu\beta\beta$ events).

Each individual optical module is made of the association between two sub-detectors, a scintillator and a photomultiplier.

Scintillators

The material chosen for the SuperNEMO scintillators is an organic, polystyrene-based material, doped with 0.05% of POPOP (1.4-bis(5-phenyloxazol-2-yl) benzene), a scintillator used as a wavelength shifter, and 1.5% of p-Terphenyl (p-TP), a secondary wavelength shifter. This composition fulfils the requirements of high light yield, low electron back-scattering (because of its low Z), high radiopurity, good timing and a relatively low cost. Four main geometries have been considered for the scintillator blocs during the R&D phase, all presented in Fig. 2.8. What all these forms have in common is that they can be stacked to form

(a) Cuboid shape 256×256 mm^2.

(b) Cuboid shape 308×308 mm^2.

(c) Tapered shape 308×308 mm^2.

(d) Hexagonal shape ⌀ 276 mm.
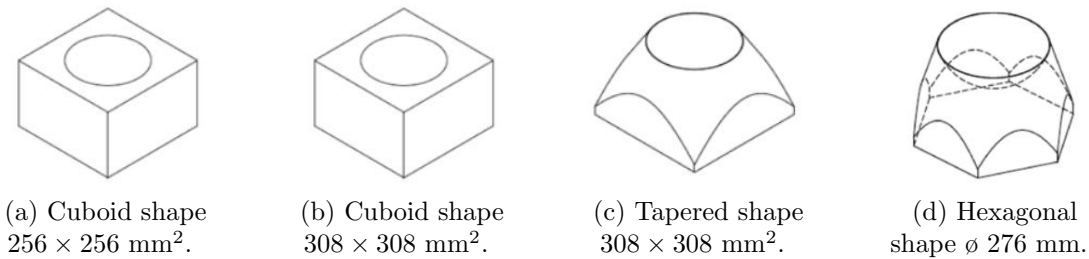
Figure 2.8: Scintillator shapes considered for the SuperNEMO demonstrator. The first one had been selected.

a compact active detection volume, thanks to their entrance face shapes. Tapered geometries have been considered in order to reduce the amount of material. The hexagonal shape was designed to get closer to a cylindrical shape and thus to limit edge effects on light propagation inside the scintillator. However, Monte-Carlo simulations and measurements were carried out, showing the best energy

resolutions are reached for hexagonal and cuboid 256×256 mm^2 shapes. As these two geometries have the same entrance face area and give similar energy resolution results, the cuboid block has been chosen for the final design to ease the manufacturing. A two dimensional drawing, as well as a picture of a cuboid scintillator is given in Fig. 2.9. The scintillator block is hollowed out to receive
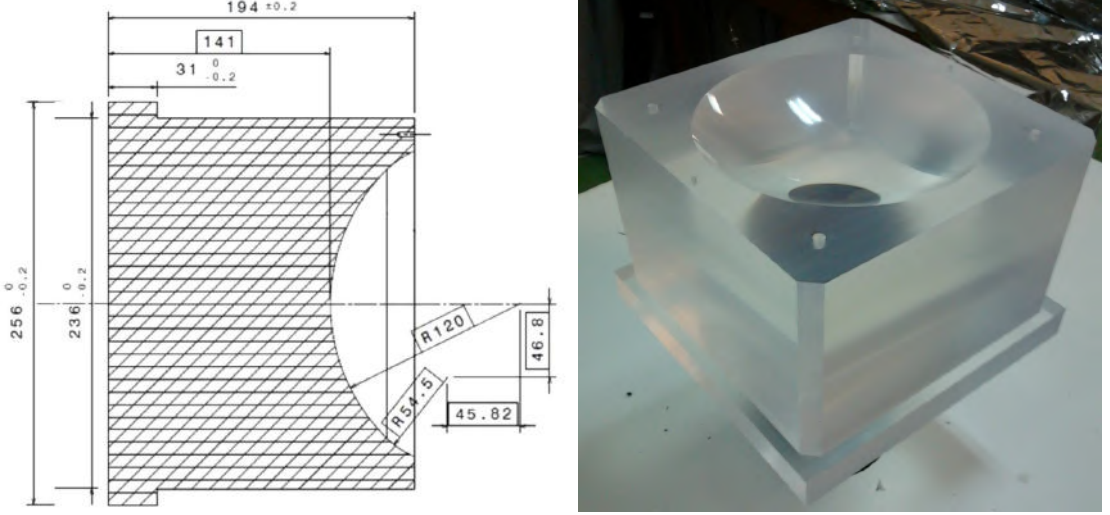
Figure 2.9: Geometry of a polystyrene cuboid scintillator block designed for the SuperNEMO demonstrator. The polystyrene is hollowed out to receive the photomultiplier bulb.

the photomultiplier bulb. To enhance the external gammas rejection by enlarging their detection in the scintillator, the SuperNEMO scintillator blocks are designed thicker compared to that of NEMO-3. In order to increase the collection light efficiency, each scintillator block is wrapped in radio-pure Teflon (on its sides) and aluminised Mylar (on its sides and front face). The latter also protects the scintillators against the UV photons coming from the tracker chamber and other surrounding optical modules.

The incoming particles (electrons, positrons or photons) enter the plastic scintillator and interact by ionisation. The scintillator thus emits scintillation photons proportionally to the deposited energy, propagating through the scintillating medium. Some of these photons are then collected by the photomultiplier photocathode.

Photomultipliers

The SuperNEMO calorimeter requires a PMT with a high quantum efficiency, a good photoelectron collection efficiency, a linear gain with energy, a high radiopurity, a good time resolution and low dark currents. The PMT used for the NEMO-3 experiment were mainly 5 inch types. For the SuperNEMO demonstrator, 8 inches PMTs (R5912-MOD Hamamatsu) were chosen in order to reduce the number of electronic channels and increase the photo-detection surface compared with its predecessor, to improve the energy measurement.

When reaching the photocathode, some of the scintillation photons are absorbed and photoelectrons are emitted through the photoelectric effect

(Fig. 2.10). These electrons drift to the first dynode under the influence of a high electric potential difference. Electrons ionise this dynode when reaching it, amplifying the number of electrons which will in turn drift into the next dynode. This drift/ionisation cascade amplifies the initial amount of charge collected by the photocathode, creating a measurable electric current (the gain is 10^6 for an 8 inches SuperNEMO PMT).
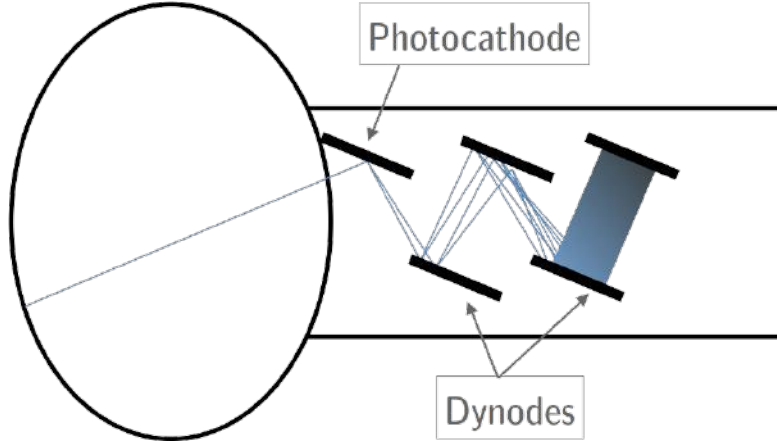
Figure 2.10: Basic operation principle of a photomultiplier. A scintillation photon enters the glass bulb of the PMT and reaches the photocathode. The photo electrons created through photoelectric effect are then multiplied by several dynodes under the influence of a high electric field.

The quantum efficiency of the chosen photomultipliers were optimised for 400 nm wave-lengths (that of the photons arriving on the photocathode) and is equal to 35% (compared to the 25% for NEMO-3). The photoelectrons collection efficiency and linearity were also improved, increasing the number of photoelectrons to ~ 1000 for 1 MeV electrons in order to reach the 8% energy resolution at 1 MeV.

Optical modules and mechanical design

Scintillators and photomultipliers are assembled together to constitute so-called *optical modules* of SuperNEMO (Fig. 2.11) by the CENBG (Bordeaux) team. They are joined together using RTV615 glue. A surface polishing and an optical gel with a refractive index comprised between the indices of the PMT glass and the scintillator also helps the optical coupling. Each optical module is protected by a magnetic shielding, whose usefulness is detailed in Sec. 3.5. Groups of 8 optical modules are pre-assembled for easy transport. Finally, the calorimeter was assembled in its entirety at LSM during the summer 2016 (Fig. 2.12).

The calorimeter of SuperNEMO is divided into three distinct sections.

- Two main calorimeter walls (one French side and one Italian side), parallel to the source foils, one on each side of the detector. Each wall is composed of 13×20 blocks, for a total of 520 optical modules. The first and last optical module rows are built with 5 inches PMTs recovered from NEMO-3, while others are 8 inches. NEMO-3 PMTs have a worse resolution than 8 inches

Figure 2.11: A scintillator coupled with a PMT. The shiny wrapping around the scintillator is the aluminised Mylar.

but they will detect almost no electrons as these rows are mainly screened by the cathode rings in front of the scintillators. However, they insure a complete coverage for the detection of γ particles.

- Gamma-Veto modules are located at the top and bottom: 2 columns of 16 on each side of the source, for a total of 64. They are only used as a veto system against γ's.

- X-walls are located on each sides of the detector: 2 columns of 16 are located on the mountain side, same on the tunnel side, for a total of 128 optical modules. As they are directly exposed to the tracker volume, they can thus detect electrons.

The optical modules constituting the X-walls and Gamma-Vetos are directly fixed on the tracker frame. As they are composed of 5 inches PMTs, their energy resolution is more modest than the rest of the calorimeter (12% FWHM at 1 MeV for the X-wall blocks and 15% FWHM at 1 MeV for the veto blocks). Nevertheless, they ensure a vital 4π calorimetric coverage for γ particles.

The commissioning of the SuperNEMO calorimeter started in 2018 and is fully achieved (a scientific paper is currently being prepared). During my thesis, I actively participated in this crucial phase for the detector development.

2.1.5 The magnetic coil and the shieldings

After a neutron capture in iron or copper, high energy gammas can be created and can cross the detector volume. Electron/positron pair creation can then occur in the source, the two emitted particles sharing the energy of the initial photon. If an electron/positron discrimination is impossible, this category of event can

(a) Back view.

(b) Front view.

Figure 2.12: Installation at LSM of one of the two main walls of the SuperNEMO calorimeter (summer 2016).

be harmful for the search for the $0\nu\beta\beta$ decay. For that reason, in the manner of NEMO-3, the SuperNEMO demonstrator will be equipped with a copper coil that will deliver a vertical (parallel to the wires) magnetic field inside the tracker chamber, in order to bend the charged particle trajectories.

The SuperNEMO magnetic field

A three-dimensional representation of the SuperNEMO demonstrator is given in Fig. 2.13 with the coil circled in red. A study led by the collaboration allowed to
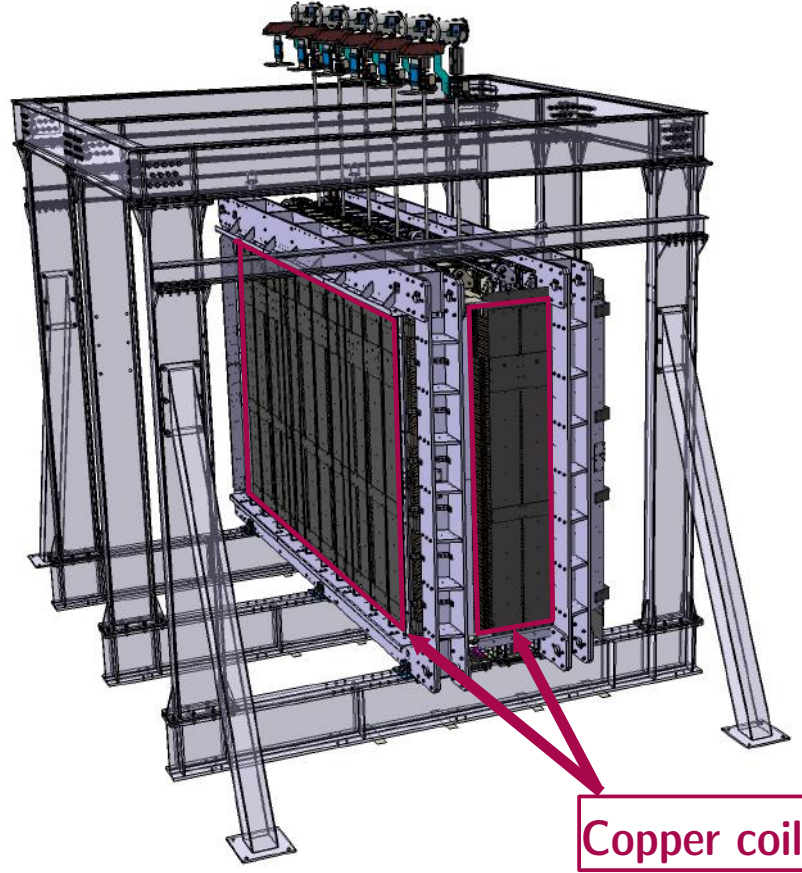
Copper coil

Figure 2.13: 3D representation of the SuperNEMO demonstrator, without the external iron shielding. The copper coil is circled in red.

determine the optimal intensity for the magnetic field would be 25 Gauss, allowing to bend the few MeV particle trajectories, thus providing a useful discrimination between electrons and positrons. It is, however, not high enough to impact significantly neither the few muons nor the α particles expected to be detected by the tracker. Due to their much higher momenta, they will instead leave straight-like tracks in the wire chamber.

The copper coil is constituted of copper rods recycled from NEMO-3 and reshaped by the mechanics team at LAL to surround the demonstrator (Fig. 2.14). The coil is made of 200 turns with 16 mm steps, which makes it possible to generate the desired magnetic field while limiting the amount of heat produced. The overall

Figure 2.14: One of the coil panel, recycled from NEMO-3.

dimensions are $6097 \times 2198 \times 3483$ mm^3 and are supported by iron plates, for a total weight of 9 tonnes. The copper coil was planned to be installed by March 2020 but was delayed due to the world health situation.

Magnetic shieldings

Unfortunately, the PMTs are highly sensitive to the presence of a magnetic field inside the detector and their performances could be greatly impacted [9][10]. Indeed, even a magnetic field as low as 1 Gauss can prevent the low energy photoelectrons from reaching the first dynode and thus impact the PMT energy resolution. Therefore, 3 mm thick pure iron shieldings have been designed to surround the optical modules and protect them from the magnetic field (Fig. 2.15). The magnetic shieldings are separated by 10 mm acrylic spacers (PMMA). As done for NEMO-3, a better magnetic shielding would have been achieved with mu-metal, but this material is much more expensive and unfortunately less radio-pure. Some of these mu-metal shields have however been recovered to protect the 5-inch PMTs from X-wall and Gamma-Vetos which are less affected by higher levels of radioactivity.

2.1.6 Calibration strategy

The SuperNEMO demonstrator is designed to have a long exposure time. In this context, calibration systems are necessary to control regularly and calibrate the response of the detector.

Source deployment system

The ^{207}Bi isotope decays almost exclusively through electron capture to excited states of ^{207}Pb. The decay is followed by ^{207}Pb de-excitation with γ-ray emission (the decay scheme is given in Fig. 2.16). The γ-ray of 1770 keV can convert in K,L

Figure 2.15: A block of 8 optical modules grouped together for installation at LSM. The magnetic shields are the black boxes surrounding the optical modules.
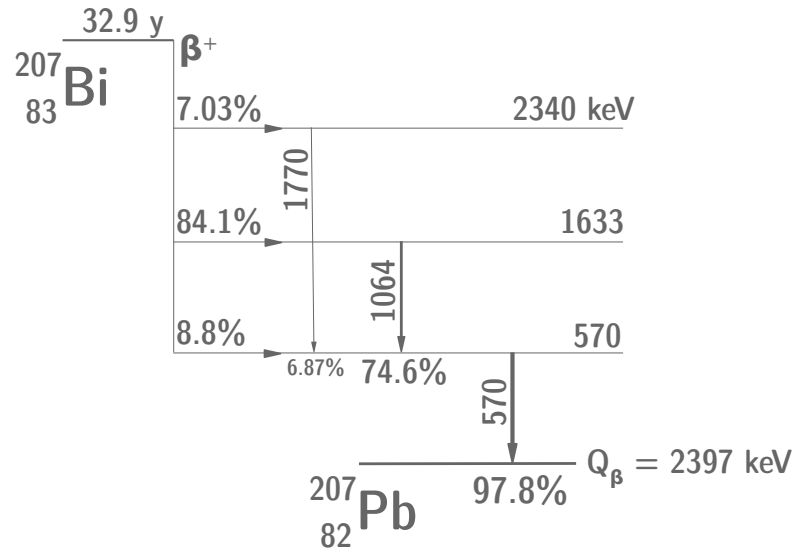
Figure 2.16: Simplified decay scheme of the ^{207}Bi isotope.

or M electrons with a given probability through the internal conversion process, which is described in detail in Chapter 4. The three corresponding electron energies are 976 keV (7.1% probability), 1050 keV (1.8% probability) and 1060 keV (0.4% probability).

Therefore, ^{207}Bi sources can be used for SuperNEMO absolute energy calibrations: the three different electrons energy peaks can be measured helping to follow and thus correct the response of the calorimeter modules with time. In total 42 sources (7 columns and 6 rows) of around 130 Bq are integrated to the so-called *deployment system*, which is in charge of the automatic deployment of the calibration sources between the source foils (Fig. 2.17). To do so, the Bismuth
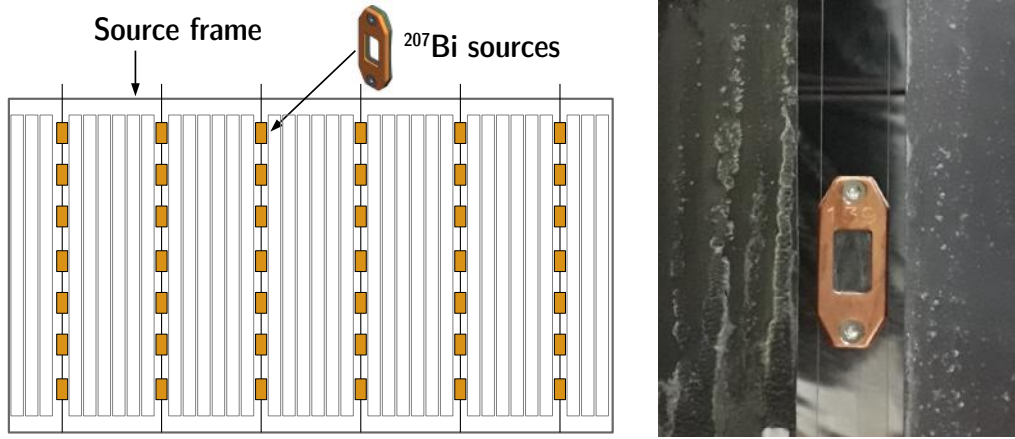
Figure 2.17: Bismuth calibration sources in the automatised deployment system. Sketch of the sources deployed (left) and picture of one of the sources, between two ITEP source foils (right).

sources are attached at seven fixed points of six different stainless steal wires. Each wire is wrapped around a wheel on top of the detector which may be rotated by a stepper motor, making it possible to introduce the sources into the detector source frame. Daily runs are being considered to monitor the gain of the conversion electron.

Light Injection System

The so-called *Light Injection* (LI) System will monitor the stability of the calorimeter response in energy during the data acquisition time (~ 2.5 years). A scheme of the complete LI calibration system is given in Fig. 2.18. Twenty
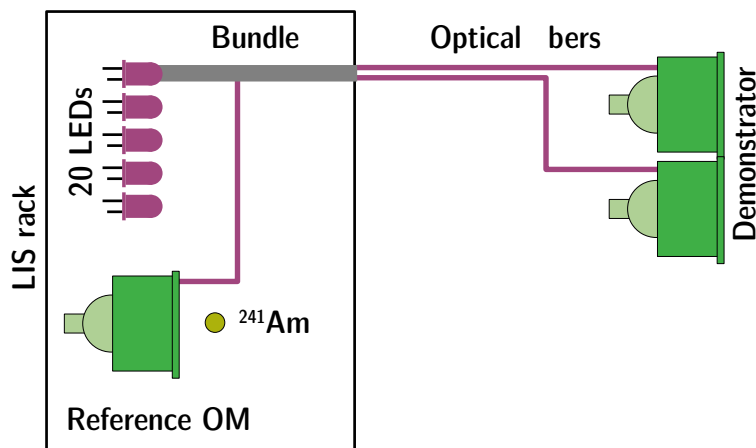
Figure 2.18: A scheme of the Light Infection (LI) calibration system. More than 1300 fibers, distributed in 20 bundles, carry the light from 20 LEDs to each scintillator block of the demonstrator. Reference OMs coupled with ^{241}Am sources monitor the LED light.

Light Emitting Diodes (LED) at 385 nm will inject light in each scintillator block via optical fibers. A set of reference optical modules, receiving light from both LEDs and ^{241}Am sources, monitors the stability of the LEDs. This system is fully installed and entered in the commissioning phase in 2019. I participated in the analysis of the first LIS commissioning data taken discussed in Chapter 6.

2.1.7 Detector cabling

During the R&D program, special attention has been paid to the total number of electronic channels needed for the demonstrator. Indeed, this number must remain reasonable in order to control the total cost of the experiment, but must be high enough so that the granularity of the detector is sufficient to search for the $0\nu\beta\beta$ decay.

Calorimeter cabling

The basic operation principle of a SuperNEMO photomultiplier have been discussed in Sec. 2.1.4. To ensure this sub-detector amplifies the signal sufficiently, a potential difference is applied between the PMT dynodes. To do so, a high voltage (HV) must be provided to the PMT. Therefore, each PMT divider is connected to a so-called *high voltage* cable. The voltage applied depends on the individual optical module characteristics and is about ~ 1500 V for the 8 inches and ~ 1100 V for the 5 inches. After the electrons have been collected on the last dynode, the charge is collected by *signal cables* sending the charge to the electronics. Finally, each PMT divider is connected to two cables, one providing the high voltage and the other ensuring the signal received by the optical module is transmitted to the electronics. A back view of one of the main calorimeter wall is given in Fig. **??**

- photo cablage, si possible cul d'un PMT

- connecteurs, dire qu'on a coupé les cables, et soudés au PMT (signal)

Tracker cabling

- dire participé install tous les cables

- routage cables

2.1.8 Electronics

Dedicated electronics have been developed for the SuperNEMO demonstrator. Six racks arranged on the electronic platform next to the detector contain all the electronics. The racks have been organised in separate areas - called crates - to accommodate the hardware dedicated to the calorimeter, tracker and calibration systems. The calorimeter electronics were realised at LAL while the tracker electronics were developed jointly by the French and English teams.
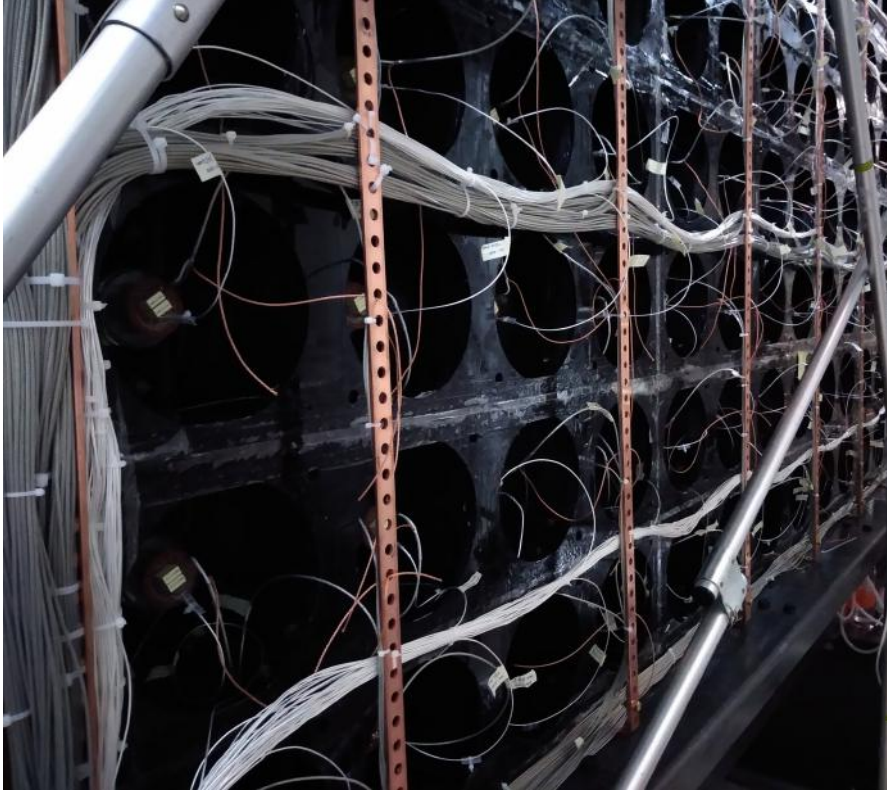
Figure 2.19: Front view of one main calorimeter wall. Signal cables are white and thin, HV cables are grey and thick.

The triggering and acquisition electronics are based on a three-levels architecture: the front-end boards (FEB), the control boards (CB) and the trigger boards (TB). From the analogue signal generated in one part of the detector to its storage, a complex communication pattern takes place between these three structures.

1. The FEBs receive, process and digitise the primary analogue signals from the optical modules and the Geiger cells. The digitisation of the pulses by the FEBs is an innovation for SuperNEMO compared to NEMO-3 where only the ADC (analogue-to-digital converter) and TDC (time-to-digital converter) were calculated. When a signal is transmitted in one of the electronic channels of the FEB, it locally synthesises digital information (such as time measurements, signal sampling, etc.). Part of this information is transmitted directly to the control board. Other data are stored in the FEBs as long as the central controller system has not validated or invalidated their acquisition. There are two types of FEBs, one for the calorimeter and one the tracker.

2. The control boards receive, centralise and forward signals coming from distinct locations of the detector (i.e. distinct FEBs). The calorimeter and tracker control boards have the same design and only differ by the firmware (i.e. how they are programmed).
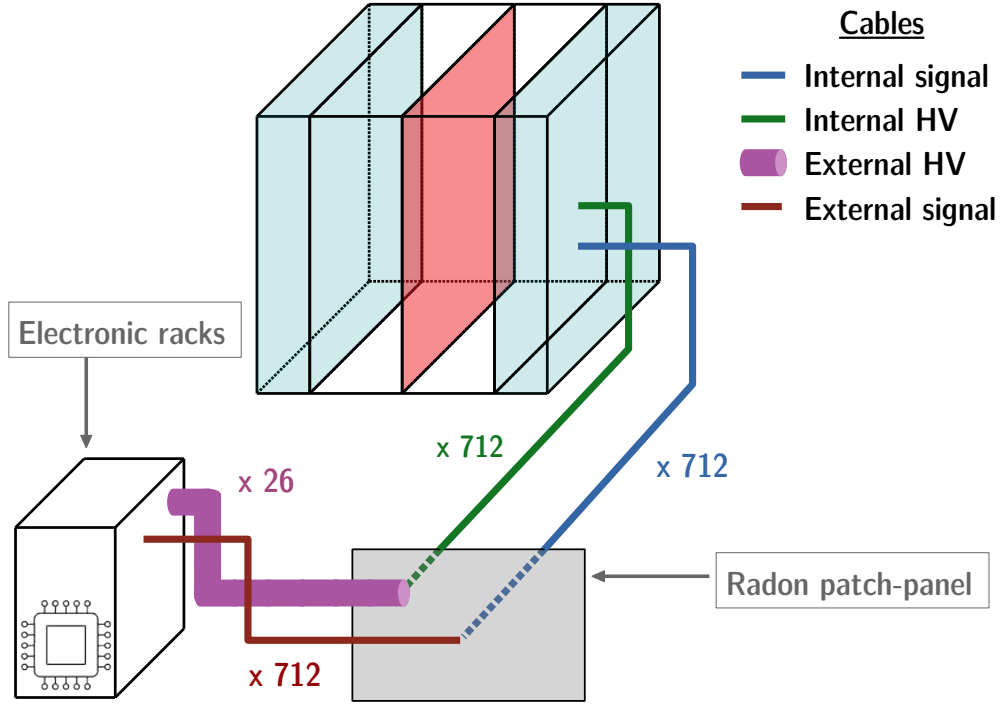
Figure 2.20: A scheme of the calorimeter cabling. Internal signal and HV cables go from the calorimeter to the patch-panel. External cables link the patch-panel to the electronic racks.

3. Once the acquisition decision is taken by the trigger board, the control boards propagate the information to calorimeter and tracker FEBs for the acquisition to begin.

4. After the acquisition has been taken, all digitised data are sent via the control boards to the data acquisition system (DAQ).

The electronics commissioning has begun in June 2018 at Manchester and is fully completed. I participated in the timing calibration of the front-end boards, which I discuss in Chapter 6.

Dedicated calorimeter electronics

In total, three crates are dedicated to the signal acquisition of the calorimeter. Each of them houses 20 front-end boards and one control board placed in the centre of the crate. A picture of one fully cabled calorimeter crate is given in Fig. 2.21. All the photomultipliers of a calorimeter wall are connected to front-end boards of a unique crate. Each front-end board collects the output PMT signals of one column of optical modules of the calorimeter wall.

- For each of the main walls, 20 front-end boards are needed, each one corresponding to 13 output PMT signals.

- For X-Walls and Gamma-Vetos, only 12 front-end boards are needed (8 for X-Walls and 4 for Gamma-Vetos). One front-end board corresponds to 16 output PMT signals.
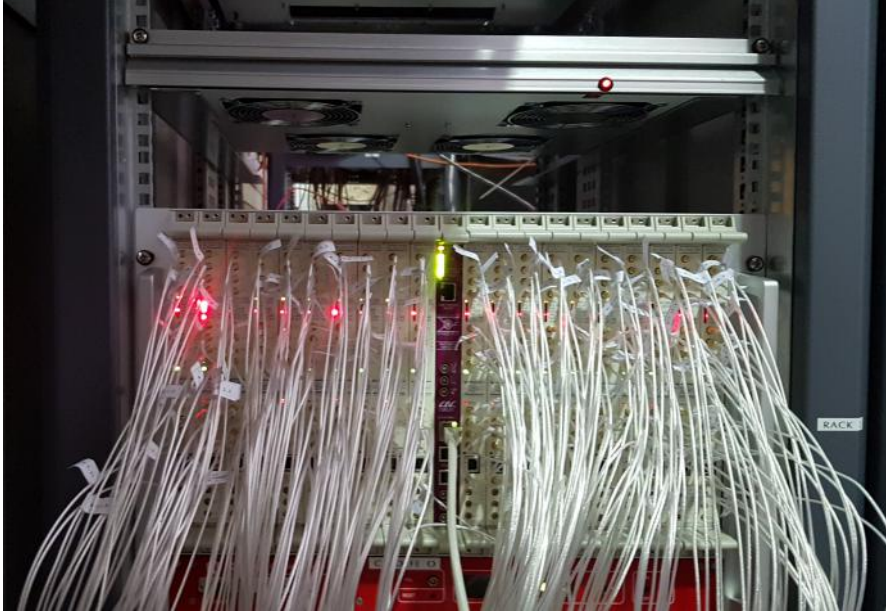
Figure 2.21: Picture of a calorimeter crate (for one of the main wall) in an electric rack.

In total, all the 52 FEBs needed for the calorimeter electronics were designed at LAL with 16 channels each, collecting all the signals from the 712 optical modules.

Dedicated tracker electronics

Three crates are dedicated to the tracker electronics, with 680 Geiger cells per crate (for a total of 2040 cells). In each crate, there are 19 tracker front-end boards, called tracker FEBs. Each FEB therefore contains 108 electronic channels. A control board is located in the centre of each crate and centralises the information from the FEBs. A total of 57 FEBs and 3 CB are then needed to collect the signal of all the anodic and cathodic analogue signal from the wire chamber.

Calibration racks

Two racks are dedicated to the electronics and informatics of the demonstrator's calibration systems (one for the deployment system, one for the light injection system).

2.1.9 Detector gas tightness

An important part of the SuperNEMO detector is filled with a Helium-based gas mixture. As described in Sec. 2.1.3 it is essential for the proper functioning of the tracker that the detector is gas tight. As with the NEMO-3 detector, a major effort is therefore made to ensure that the detector is sealed to prevent external contaminants from infiltrating. Different techniques are deployed during and after the detector assembly (Fig. 2.22).
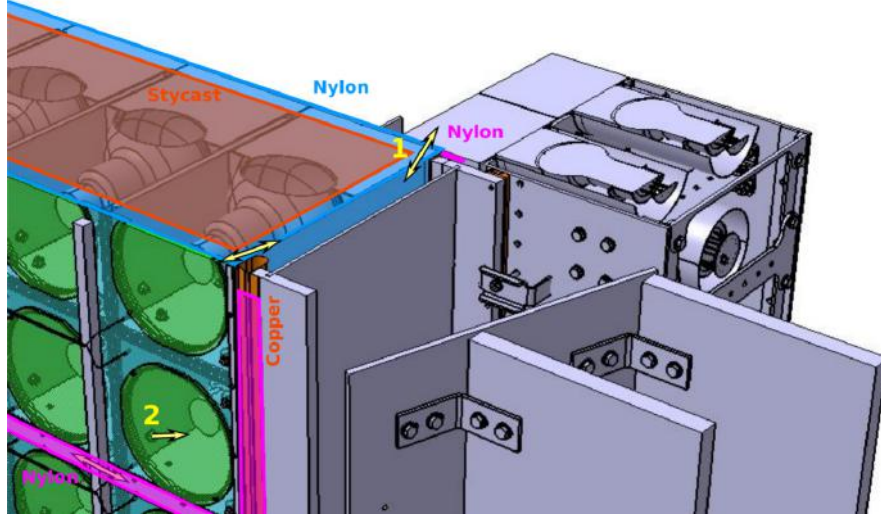
Figure 2.22: Demonstrator gas tightness plan. Back view of one of the calormieter main walls.

- The pre-assembled blocks of 8 optical modules were wrapped in a radiopure nylon film. Additional patches of nylon film were glued on the calorimeter back side on each gap between these groups of 8 optical modules.

- After the calorimeter walls assembly, copper bars have been installed on the back side at the gap between the calorimeter and the structure supporting the detector.

- A piece of nylon was mounted on the front side of each main wall before the detector was closed (Fig. 2.23).

- Different leak-sealing radiopure materials (SBR, RTV, Stycast and Black Mamba glues) have been applied on different detector areas (mainly inside the optical module shieldings, tracker frame and source frame).

I took part in several of these operations, and my first shift to Modane was one of them.

After these operations, remaining leaks can still occur through two interfaces:

- through the nylon film. Unfortunately, one of the two films (Italian side) were damaged during the detector closure leading to possible gas leaks between the tracker volume and the optical modules buffer volume,

- through optical module shieldings leading to leaks between the buffer volume and outside the detector.

In order to reduce these leaks, several sealing operations have been carried out. They consist in injecting a gas inside the tracker via the gas injection system and detect possible leaks with a gas probe. In case of major leaks, helium gas could infiltrate the PMTs vacuum by diffusing through the glass. Therefore the gas chosen for the first leaks checks is Argon. Every major leak is then fixed using the more suitable radiopure glues presented above (depending on the size and location

Figure 2.23: Piece of radiopure nylon film installed on the front face of each calorimeter main walls.

of the leak). The first over-pressure in the tracker was successfully obtained in September 2019. After all major leaks were detected, Helium can be injected inside the tracker to identify smaller leaks without any danger for the PMTs.

2.2 Backgrounds

The SuperNEMO experiment seeks, if it exists, an extremely rare signal. It is therefore necessary to know and reduce as much as possible the possible sources of background that could degrade the observation of the signal in question. The energies involved in the double beta process imply that this type of experiment is sensitive to several sources of background.

2.2.1 Internal background

We refer to *internal background* as the background being generated from inside the sources, where trace quantities of naturally-occurring radioactive isotopes can occasionally produce two-electron events and thus can mimic $\beta\beta$-decay events. The largest contributions come from isotopes of decay chains of ^{238}U and ^{232}Th.

Two-electrons signature processes

Following a beta disintegration, mainly three processes are likely to mimic a double beta disintegration with two electrons exiting the source foil as a signature, as shown in Fig. 2.24.
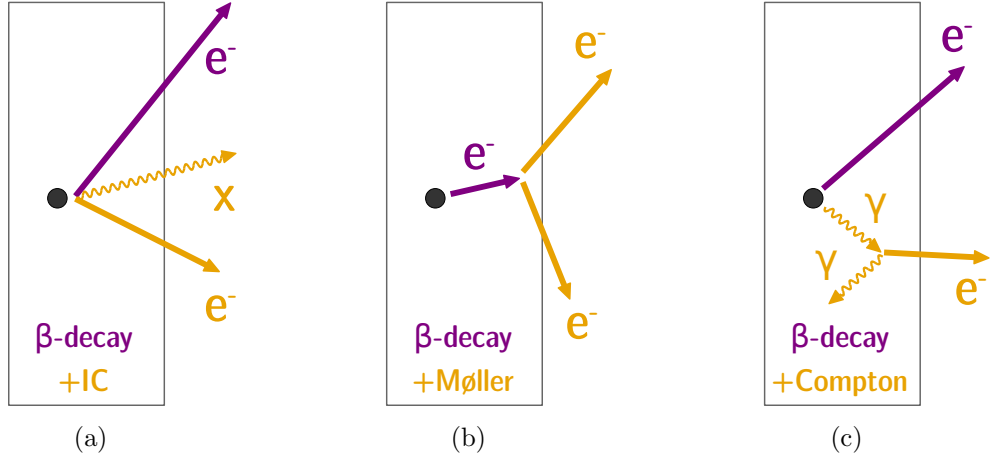
41

Figure 2.24: (a) β decay + internal conversion: radioactive nucleus performs a β decay, then an electron is emitted after internal conversion of the γ-ray. (b) β decay + Møller: (c) β decay + Compton diffusion: radioactive nucleus β decays to an excited state, then the photon performs a Compton diffusion.

- An electron resulting from an internal conversion is ejected from the atom in addition to the electron beta. An X-photon can also be emitted without being detected by the calorimeter. This process will be described in detail in Chapter 4.

- The initially emitted electron can scatter, called Møller scattering, and thus emit a second electron of significant energy.

- The photon can eject an electron from the source by the Compton effect. If the scattered photon is not detected in the calorimeter, this decay may present a two-electron signature.

Characterisation of background in the one electron and $n\gamma$ channel

The ^{208}Tl and ^{214}Bi contaminations inside the source foils is one of the harmul backgrounds for the neutrinoless double beta decay. One of the key features of the SuperNEMO demonstrator remains its ability to measure its own background in dedicated channels, which are independent from the main signal channels.

After a β disintegration, ^{208}Tl emits between 1 and 3 γ's. Consequently, the $1e1\gamma$, $1e2\gamma$ and $1e3\gamma$ channels can be used to discriminate internal ^{208}Tl events, and measure the activity of the source. For ^{214}Bi disintegrations, between 0 and 2 γ's are expected after the β decay thus a significant contribution to the $1e1\gamma$ and $1e2\gamma$ channels is also expected from ^{214}Bi.

Internal activities

Specified contamination levels have been established in order to achieve the $0\nu\beta\beta$ half-life target of $\sim 1 \times 10^{26}$ years for the final detector. The ^{82}Se demonstrator source is segmented in 34 foils, whose production was the responsibility of different laboratories (Dubna, LAPP and Tomsk). The sources have undergone different

purification treatments, in order to investigate new techniques, and to compare them with those of NEMO-3. After the sources production and purification, preliminary measurements have been performed with the BiPo-3 detector to determine the actual ^{208}Tl and ^{214}Bi contamination levels inside the foils [11]. The level of radon emissions inside the tracker was also measured by the collaboration, for each of the four sections of the chamber, using a concentration line. We summarise all these contamination levels in Tab. 2.3, and give a comparison with the detector initial specifications. The targeted ^{208}Tl level is not reached, being

	Specified activities	Measured activities
^{208}Tl	$2\,\mu$Bq.kg^{-1}	$54\,\mu$Bq.kg^{-1} [26 - 102]
^{214}Bi	$10\,\mu$Bq.kg^{-1}	$< 290\,\mu$Bq.kg^{-1}
^{222}Rn	0.15 mBq.m^{-3}	0.15 ± 0.02 mBq.m^{-3}

Table 2.3: Measured and specified activities for the SuperNEMO demonstrator. The ^{222}Rn tracker contamination is measured with a concentration line [12], extrapolated with a 2 m^3/h flow rate. The limit on ^{214}Bi contamination is provided by BiPo measurements for a 90% CL [11].

almost 27 times higher than expected, and 3.0×10^4 internal Thallium events are expected in 2.5 years. Nevertheless, on average, the activity of the sources was improved by a factor of 2 compared to the ^{100}Mo sources of NEMO-3. In addition, valuable information has been accumulated on the different production techniques, which are of great importance for the final detector construction. In particular, the two best ^{208}Tl sources activities were reached by inverse chromatography, reaching a $20 \pm 10\,\mu$Bq/kg level, an improvement by a factor 5 compared to NEMO-3. This encourages for further investigations in this direction. The sensitivity of BiPo detector only allowed to give an upper limit on the level of internal ^{214}Bi (an activity of 290 μBq/kg would correspond to 1.6×10^5 internal Bismuth events in 2.5 years). Precise measurements are expected from the demonstrator calibration. Radon emissions from the tracker were also measured, and extrapolated with an air flow rate of 2 m^3/h inside the chamber, showing the targeted level of 0.15 mBq.m^{-3} was reached.

2.2.2 External background

2.2.3 Radon background

- Décire la contamination mesurée des sources, et du radon

- les sources de Radon: 1) contamination du gaz en entrée du tracker 2) émanation des matériaux du tracker 3) diffusion du radon depuis le détecteur vers le tracker 4) diffusion du radon depuis le laboratoire vers le tracker et des moyens qu'on a de s'en prémunir 1) passage du gaz (hors alcool) dans un piège à radon 2) mesure en émanation des matériaux du tracker avec la concentration line, augmentation de flux du gaz pour avoir un niveau de Radon suffisamment bas. 3) feuille Nylon pour éviter la diffusion du radon du calorimètre vers le tracker 4) tente anti-radon

- Radon is a noble gas which occurs as an indirect decay product of uranium and thorium. Due to its chemical properties, radon has a long diffusion length in solids, making it difficult to remove. Radon contaminations inside the tracker volume is a major background to the rare event experiments such as SuperNEMO. Simulations show that, to achieve the designed sensitivity, the level of radon must not exceed 0.15 mBq/m^3 since its decay daughter ^{214}Bi, $Q_{\beta\beta} = 3.2$ MeV can mimic a $0\nu\beta\beta$ event. Radon concentration measurements inside the demonstrator tracker have been performed by the SuperNEMO collaboration, revealing an activity of 0.15 ± 0.02 mBq/m^3, through the combination of an anti-radon tent and an air-flushing method.

- They are outgased in the air from the rock walls of the experimental hall and can enter the detector either through tiny gaps between sectors or through gas pipe joints. The progeny of radon and thoron produces γ-rays and β decays accompanied by internal conversion (IC), Møller or Compton scattering.

- parler des mesures de bdf externe (PMT, cerdric)

2.2.4 Background reduction

2.2.4.1 Radiopurity

Specifications

BiPo measurements

Radon suppression system

The underground laboratory

External shield

- patch panel

- gas tightness

2.3 The SuperNEMO software

2.3.1 Simulation

- montrer visu

As described in Sec. 2.3 of Chapter 2, the SuperNEMO collaboration developed its own simulation, reconstruction and analysis environment. The Falaise software, specifically designed by and for the SuperNEMO collaboration, holds the `C++` library for the event reconstruction and analysis of simulated and real data. Especially, it contains the geometry, the detector material, the event data model, the reconstruction algorithms and the data analysis. Finally, the SNFee software is a tool package for the configuration, control and monitoring of the SuperNEMO front-end electronics.

2.3.2 Reconstruction

Particle identification with detector scheme

2.3.3 Monte-Carlo simulations

2.3.4 Analysis chain

2.3.5 Modifications of simulation software

2.4 Analysis tools

2.4.1 Internal probability

Internal probability is a mathematical tool used to quantify the probability that two particles were emitted simultaneously and at the same location in the source foils. This tool is based on the particle Time-Of-Flight computation. Firstly, we define, for two particles, the internal χ^2

$$\chi^2_{int} = \frac{((t_1^{exp} - t_1^{th}) - (t_2^{exp} - t_2^{th}))^2}{\sigma^2_{tot}} \,. \tag{2.1}$$

t_i^{th} is the theoretical time of arrival of the particle i inside the calorimeter, t_i^{exp} the arrival time experimentally measured, c is the speed of light, and σ_{tot} is the quadratic sum of all uncertainties. The theoretical time, is defined as

$$t_i^{th} = \frac{L_i}{\beta_i \, c} \,, \tag{2.2}$$

where L_i is the reconstructed track length, and β_i corresponds to

$$\beta_i = \frac{\sqrt{E_i(E_i + 2m_i)}}{E_i + m_i} \,, \tag{2.3}$$

E_i being the energy of the particle and m_i its mass. The total uncertainty, σ_{tot}, is defined as

$$\sigma_{tot} = \sqrt{\sigma^2_{t_1} + \sigma^2_{t_2} + \sigma^2_{\beta_2} + \sigma^2_{\beta_1} + \sigma^2_{l_1} + \sigma^2_{l_2}} \,. \tag{2.4}$$

We compare the experimental time difference to the theoretical time difference, to see if it can be explained only by the difference in track lengths. If it is compatible, which means of the order of the experimental uncertainties, the associated χ^2 will be low i.e. close to 1 or lower.

The uncertainty σ_t on the time measurement This term is directly related to the phenomenon of absorption and re-emission of scintillation photons detailed in Chapter 6. It is defined as

$$\sigma_t = \sqrt{\frac{\tau^2_{SC} + \left(\frac{FWHM_{TTS}}{2\sqrt{2\ln 2}}\right)^2}{N_{PE}}} \,, \tag{2.5}$$

where τ_{SC} is the scintillator characteristic time, due to the scintillator de-excitation time: it corresponds to the time emission of the scintillation photon responsible for the creation of the photoelectron on the photocathode. $\mathrm{FWHM_{TTS}}$ is the temporal dispersion linked to the photomultiplier: the transit time of the photoelectrons inside the photomultiplier can evolve, according to its point of creation on the photocathode. This transit time is unique for each photomultiplier, and has to be characterise experimentally. For the SuperNEMO scintillators, $\tau_{\mathrm{SC}} = 2.5$ ns [?] and $\mathrm{FWHM_{TTS}} = 2.25$ ns [?]. $\mathrm{N_{PE}}$ is the number of photo-electrons emitted after a particle has deposited all its energy E in the scintillator:

$$\mathrm{N_{PE}} = E \times \left(\frac{2\sqrt{2\ln 2}}{\mathrm{FWHM_E}} \right)^2 , \tag{2.6}$$

where $\mathrm{FWHM_E}$ is the energy resolution of the PM, 8 % at 1 MeV for the SuperNEMO calorimeter. Therefore, for a particle of 1 MeV depositing all its energy inside a scintillator, $\mathrm{N_{PE}} \sim 866$ photo-electrons are emitted, an improvement of ? % compared with NEMO-3. Finally, the uncertainty σ_t on the time measurement can be estimated thanks to a relative calibration of the PMs, and depends on the incoming particle nature (photon or electron). Preliminary studies gave a first estimation of this parameter [13] and found $\sigma_t = 342 \pm 10$ ps for 1 MeV gammas entering the front face of the scintillator, and $\sigma_t = 248 \pm 6$ ps for 1 MeV electrons. On the occasion of the SuperNEMO detector commissioning, we finalise this study and characterise the calorimeter time resolution in Chapter 5.

The uncertainty σ_β on the particle energy This term is derived from Eqs. (2.2) and (2.3):

$$\sigma_{\beta_i} = \frac{t_i^{th} \times m_i^2}{E_i \times (E_i + m_i) \times (E_i + 2m_i)} \times \sigma_E , \tag{2.7}$$

where $\sigma_E = \mathrm{FWHM_E} \times \sqrt{E_i}$ represents the energy resolution of the PM for the energy E_i.

The uncertainty σ_L on the reconstructed track length This corresponds to the typical uncertainty due to particles track reconstructions, due to the uncertainty on the interaction point inside the scintillator block. This uncertainty is greater for γ particles than for electrons. Indeed, thanks to the gaseous detector and the trajectory fitting, valuable informations on the impact point inside the scintillator are provided for electrons crossing the tracker, while photons only deposit their energy inside the calorimeter, without ionising the tracker gas. In the framework of the optimisation of γ reconstruction in the SuperNEMO detector, a previous study has evaluated the uncertainty on the track length for γ's, by simulating mono-kinetic γ's, and estimated $\sigma_L = 0.9$ ns [9]. The value used in the simulation/reconstruction pipeline, for the case of electrons, is inherited from the NEMO-3 analysis with $\sigma_L = 0.1$ ns. An optimisation of this parameter is given in Chapter 4.

We would translate the internal χ^2 distribution into the so-called *internal probability* through

$$P_{int} = \frac{1}{N} \int_{\chi_{int}^2}^{+\infty} x^{-\frac{1}{2}} e^{-\frac{x}{2}} dx \, , \tag{2.8}$$

with N the normalisation factor. This formula transforms the χ^2 Gaussian distribution into a flat distribution between 0 and 1. One of the benefits of using the probability distribution rather than the χ^2 distribution is that it brings extra qualitative information, especially useful to check the estimation of the uncertainties. The shape of the probability distribution can bring out an overestimation or an underestimation of the uncertainties, which would translate into a positive or a negative slope, respectively. On the other hand, a flat distribution signifies an appropriate estimation of the errors and confirms the Gaussian distribution of the original quantity measured.

2.4.2 External probability

2.5 Goals and comparison with NEMO-3

- Expected sensitivity

2.6 Conclusion

Bibliography

[1] M. Agostini et al. Probing majorana neutrinos with double-β decay. *Science 365*, 1445, 2019.

[2] S.I. Alvis et al. Search for neutrinoless double-beta decay in ^{76}ge with 26 kg-yr of exposure from the majorana demonstrator. *Phys. Rev. C*, 100, 2019.

[3] O. Azzolini et al. First result on the neutrinoless double-β decay of ^{82}Se with cupid-0. *Phys. Rev. Lett.*, 120:232502, Jun 2018.

[4] C. Alduino et al. First results from cuore: A search for lepton number violation via $0\nu\beta\beta$ decay of ^{130}Te. *Phys. Rev. Lett.*, 120:132501, Mar 2018.

[5] J. B. Albert et al. Search for neutrinoless double-beta decay with the upgraded exo-200 detector. *Phys. Rev. Lett.*, 120:072701, Feb 2018.

[6] A. Gando et al. Search for majorana neutrinos near the inverted mass hierarchy region with kamland-zen. *Phys. Rev. Lett.*, 117:082503, Aug 2016.

[7] Chopra A. C0 commissioning results. Internal presentation, 2015.

[8] Cerna C. Tracker review conclusions. Internal presentation, 2014.

[9] S. Clavez. *Development of reconstruction tools and sensitivity of the SuperNEMO demonstrator*. PhD thesis, Université Paris Sud, 2017.

[10] Garrido X. Bongrand M. Hamamatsu 8" pmt test in magnetic shield. Internal presentation, 2014.

[11] Loaiza P. Source foils measurement with bipo. Internal presentation, 2017.

[12] Xin Ran Liu. Radon mitigation strategy and results for the supernemo experiment. IoP APP / HEPP Conference, 2018.

[13] A. Huber. *Recherche de la nature du neutrino avec le détecteur SuperNEMO : Simulations optiques pour l'optimisation du calorimètre et performances attendues pour le ^{82}Se*. PhD thesis, Université Bordeaux, 2017.

[14] R. Arnold et al. Probing new physics models of neutrinoless double beta decay with supernemo. *Eur. Phys. J. C*, 2010.

[15] Tretyak V.I. Ponkratenko O.A. and Zdesenko Yu.G. The event generator decay4 for simulation of doublebeta processes and decay of radioactive nuclei. *Phys. At. Nucl.*, 63:1282–1287, Jul 2000.

[16] R. Arnold et al. Results of the search for neutrinoless double-β decay in ^{100}mo with the nemo-3 experiment. *Phys. Rev. D*, 2015.

[17] Perrot F. Radiopurity measurements for 8" pmts and preliminary budget for the sn demonstrator. Internal presentation, 2017.

[18] Gomez-Cadenas et al. Physics case of supernemo with ^{82}se source. Internal presentation, 2008.

[19] R. Arnold et al. Final results on ^{82}se double beta decay to the ground state of ^{82}kr from the nemo-3 experiment. *Eur. Phys. J. C*, 2018.

[20] Cousins D. Feldman G. A unified approach to the classical statistical analysis of small signals. *Phys.Rev.*, pages 3873–3889, 1999.

[21] J. Kotila and F. Iachello. Phase-space factors for double-β decay. *Phys. Rev. C*, 85:034316, Mar 2012.

[22] J. Menéndez et al. Disassembling the nuclear matrix elements of the neutrinoless $\beta\beta$ decay. *Nuclear Physics A*, 818(3):139 – 151, 2009.

[23] Y. Iwata et al. Large-scale shell-model analysis of the neutrinoless $\beta\beta$ decay of ^{48}Ca. *Phys. Rev. Lett.*, 116:112502, Mar 2016.

[24] J. Barea, J. Kotila, and F. Iachello. $0\nu\beta\beta$ and $2\nu\beta\beta$ nuclear matrix elements in the interacting boson model with isospin restoration. *Phys. Rev. C*, 91:034304, Mar 2015.

[25] J. Hyvärinen and J. Suhonen. Nuclear matrix elements for $0\nu\beta\beta$ decays with light or heavy majorana-neutrino exchange. *Phys. Rev. C*, 91:024613, Feb 2015.

[26] F. Šimkovic et al. $0\nu\beta\beta$ and $2\nu\beta\beta$ nuclear matrix elements, quasiparticle random-phase approximation, and isospin symmetry restoration. *Phys. Rev. C*, 87:045501, Apr 2013.

[27] Tomás R. Egido J. Luis Vaquero López N., Rodríguez. Shape and pairing fluctuation effects on neutrinoless double beta decay nuclear matrix elements. *Phys. Rev. Lett.*, 111:142501, Sep 2013.

[28] J. M. Yao, L. S. Song, K. Hagino, P. Ring, and J. Meng. Systematic study of nuclear matrix elements in neutrinoless double-β decay with a beyond-mean-field covariant density functional theory. *Phys. Rev. C*, 91:024316, Feb 2015.

[29] P. K. Rath, R. Chandra, K. Chaturvedi, P. K. Raina, and J. G. Hirsch. Uncertainties in nuclear transition matrix elements for neutrinoless $\beta\beta$ decay within the projected-hartree-fock-bogoliubov model. *Phys. Rev. C*, 82:064310, Dec 2010.

[30] Dong-Liang Fang, Amand Faessler, Vadim Rodin, and Fedor Šimkovic. Neutrinoless double-β decay of deformed nuclei within quasiparticle random-phase approximation with a realistic interaction. *Phys. Rev. C*, 83:034320, Mar 2011.

[31] A. Chapon. *Mesure des processus de double désintégration bêta du Mo vers l'état excité 0_1^+ du Ru dans l'expérience Nemo3, Programme de R&D SuperNEMO : mise au point d'un détecteur BiPo pour la mesure de très faibles contaminations de feuilles sources.* PhD thesis, Université Caen Basse-Normandie, 2011.

[32] Snow S. A magnetic field map for the tracker. Internal presentation, 2015.

[33] A. Pin. *Recherche de la nature du neutrino via la décroissance double bêta sans émission de neutrinos. Caractérisation et optimisation du calorimètre SuperNEMO et impact sur la recherche de la décroissance du 82Se Développement du premier prototype LiquidO.* PhD thesis, Université Bordeaux-Gradignan, 2020.

[34] A. H. Wapstra G. Audi. The 1995 update to the atomic mass evaluation. *Nucl. Phys. A*, 595:409–480, feb 1995.

[35] R. Arnold et al. Measurement of the $2\nu\beta\beta$ decay half-life of ^{150}nd and a search for $0\nu\beta\beta$ decay processes with the full exposure from the nemo-3 detector. *Phys. Rev. D*, 94, oct 2016.

[36] Nucleid database.